



# Colloidal dynamics over a tilted periodic potential: Nonequilibrium steady-state distributions

Xiao-guang Ma,<sup>1,\*</sup> Pik-Yin Lai,<sup>2,3,†</sup> Bruce J. Ackerson,<sup>4,‡</sup> and Penger Tong<sup>1,§</sup>

<sup>1</sup>*Department of Physics, Hong Kong University of Science and Technology, Clear Water Bay, Kowloon, Hong Kong*

<sup>2</sup>*Department of Physics and Center for Complex Systems, National Central University, Chungli, Taiwan 320, R.O.C.*

<sup>3</sup>*Physics Division, National Center for Theoretical Sciences, Kuang Fu Road 101, Hsinchu, Taiwan 300, R.O.C.*

<sup>4</sup>*Department of Physics, Oklahoma State University, Stillwater, Oklahoma 74078, USA*

(Received 14 January 2015; published 13 April 2015)

We report a systematic study of the effects of the external force  $F$  on the nonequilibrium steady-state (NESS) dynamics of the diffusing particles over a tilted periodic potential, in which detailed balance is broken due to the presence of a steady particle flux. A tilted two-layer colloidal system is constructed for this study. The periodic potential is provided by the bottom-layer colloidal spheres forming a fixed crystalline pattern on a glass substrate. The corrugated surface of the bottom colloidal crystal provides a gravitational potential field for the top-layer diffusing particles. By tilting the sample at an angle  $\theta$  with respect to the vertical (gravity) direction, a tangential component of the gravitational force  $F$  is applied to the diffusing particles. The measured NESS probability density function  $P_{ss}(x, y)$  of the particles is found to deviate from the equilibrium distribution  $P(x, y)$  to a different extent, depending on the driving or distance from equilibrium. The experimental results are compared with the exact solution of the one-dimensional (1D) Smoluchowski equation and the numerical results of the 2D Smoluchowski equation. From the obtained exact solution of the 1D Smoluchowski equation, we develop an analytical method to accurately extract the 1D potential  $U_0(x)$  from the measured  $P_{ss}(x)$ . This work demonstrates that the tilted periodic potential provides a useful platform for the study of forced barrier-crossing dynamics beyond the Arrhenius-Kramers equation.

DOI: [10.1103/PhysRevE.91.042306](https://doi.org/10.1103/PhysRevE.91.042306)

PACS number(s): 82.70.Dd, 05.10.Gg, 05.40.-a

## I. INTRODUCTION

Colloidal monolayers suspended at a liquid-liquid (or liquid-air) interface or near a liquid-solid interface have served as model systems to study a range of interesting problems of phase transition kinetics and dynamics in two-dimensional (2D) soft matter systems [1,2]. Examples include 2D crystallization [3,4] and grain-boundary fluctuations [5], crystal sublimation [6] and colloidal glasses [7,8], interactions between similarly charged particles [9–12], and Brownian dynamics at liquid interfaces [13–17]. They offer many advantages over atomic or molecular fluids, because the dynamics of the particles are slower and can be tracked at the single-particle level with video microscopy [18].

In a recent experiment [19], we developed a two-layer colloidal system and used it to study the diffusive barrier-crossing dynamics over a periodic potential. The periodic potential is provided by the bottom layer of colloidal spheres forming a crystalline pattern on a glass substrate. The corrugated surface of the colloidal crystal provides a gravitational potential  $U_0(x, y)$  for the diffusing particles on the top layer. The value of  $U_0(x, y)$  is determined by the size of the particles in both layers. Using the techniques of optical microscopy and multiparticle tracking, we measured the population statistics of the diffusing particles and constructed the potential  $U_0(x, y)$  via the Boltzmann distribution [20],

$$P(x, y) \sim e^{-U_0(x, y)/k_B T}, \quad (1)$$

where  $k_B T$  is the thermal energy of the diffusing particles. The dynamical properties of the diffusing particle, such as its escape time and diffusion coefficient, were simultaneously measured from the particle's trajectories. With the simultaneously obtained energetics and dynamics information, we tested the theory and demonstrated the applications of the colloidal potential.

With the capability of simultaneously tracking the particle's motion at the single-particle level and measuring the external potential, the two-layer colloidal system provides a useful platform for the study of a range of interesting problems associated with the diffusive and force-assisted barrier-crossing dynamics over complex energy landscapes. Here an external potential field is used to mimic the effect of an energy landscape, which is usually imposed by the surrounding molecules to a test particle. Similar attempts have also been made in the study of colloidal transport and diffusion in a 1D optical trap (optical tweezers) with either a periodic or random variation of the laser light intensity [21–24]. Understanding the effect of the external force on thermally activated kinetics is a concern of a common class of transport problem, such as particle separation by electrophoresis [25,26], electromigration of atoms on the surface of metals [27] and semiconductors [28], motion of a three-phase contact line under the influence of an unbalanced capillary force [29], control of crystal growth [30], and design of nanoscale machineries [31,32]. In biology and biophysics, force-assisted thermal activation is employed in various single-molecule stretching experiments to study the binding and folding energy landscape of biomolecules, such as DNA [33], RNA [34], nucleic acids [35], receptors and ligands [36], and proteins [37], and the adhesion between biomembranes of vesicles, capsules, and living cells [38,39].

More recently, we carried out a systematic study of the effects of an external force  $F$  on the barrier crossing dynamics

\*hillxgm@gmail.com

†pylai@phy.ncu.edu.tw

‡bruce.ackerson@okstate.edu

§pengert@ust.hk

of the diffusing particles over a periodic potential [40]. By tilting the entire two-layer system at an angle  $\theta$  with respect to the vertical (gravity) direction, a tangential component of the gravitational force  $F$  is applied to the top-layer particles. In the experiment, we measured the particle's mean drift velocity  $v(F, E_b)$  and diffusion coefficient  $D(F, E_b)$  as a function of  $F$  (by varying the tilt angle  $\theta$ ) and the energy barrier height  $E_b$  (by using different colloidal samples). The measured  $v(F, E_b)$  and  $D(F, E_b)$  agree well with the exact results of the 1D drift velocity [41] and diffusion coefficient [42,43]. Based on these exact results, we showed analytically and verified experimentally that there exists a scaling region, in which  $v(F, E_b)$  and  $D(F, E_b)$  both have an Arrhenius-Kramers-like form,  $v'(F) \exp[-E_b^*(F)/k_B T]$ , where the Arrhenius prefactor  $v'(F)$  and the effective energy barrier height  $E_b^*(F)$  are both modified by the external force  $F$ .

In this paper, we report a systematic study of the effects of the external force  $F$  on the nonequilibrium steady-state (NESS) dynamics of the top-layer particles over the tilted periodic potential, in which detailed balance is broken due to the presence of a steady particle flux. As a result, the measured NESS probability density function (NESS-PDF)  $P_{ss}(x, y)$  of the particles deviates from the equilibrium distribution  $P(x, y)$  as shown in Eq. (1) to a different extent, depending on the driving or distance from equilibrium. The experimental results are compared with the exact solution of the 1D Smoluchowski equation and the numerical results of the 2D Smoluchowski equation. From the obtained exact solution of the 1D Smoluchowski equation, we develop an analytical method to accurately extract the 1D potential  $U_0(x)$  from the measured  $P_{ss}(x)$ .

The remainder of the paper is organized as follows. We first present, in Sec. II, the exact solution of  $P_{ss}(x)$  obtained from the 1D Smoluchowski equation and the numerical results of  $P_{ss}(x, y)$  from the 2D Smoluchowski equation. The experimental procedures and image processing methods are presented in Sec. III. The experimental results and discussion are given in Sec. IV. Finally, the work is summarized in Sec. V.

## II. THEORY

### A. One-dimensional analytical results

We consider the 1D motion of a Brownian particle of mass  $m$  over an external potential  $U(x)$ , which can be described by the Langevin equation [20,44]

$$m \frac{d^2 x}{dt^2} + \xi \frac{dx}{dt} = f_B(t) - \frac{dU(x)}{dx}, \quad (2)$$

where  $x(t)$  is the particle's position at time  $t$ ,  $\xi dx/dt$  is the drag force experienced by the particle with  $\xi$  being the friction coefficient, and  $f_B(t)$  is the random Brownian force due to thermal fluctuations of the surrounding fluid. The last term,  $-dU(x)/dx$ , is the conservative force experienced by the particle resulting from the potential  $U(x)$ . If the motion is over-damped, which is the case for colloidal particles in an aqueous solution, the first term in the left-hand side of Eq. (2) can be omitted. When there is a constant force  $F$  acting on the particle and the potential  $U_0(x)$  without forcing is periodic, one can find exact results for the mean drift velocity [41] and diffusion coefficient [42,43]. In this case, one has

$U(x) = U_0(x) - Fx$ , where  $U_0(x) = U_0(x + \lambda)$  with  $\lambda$  being the period. The introduction of the external force  $F$  breaks the detailed balance and generates a net particle flux along the direction of  $F$ .

We now consider the probability distribution function (PDF)  $P(x, t; x_0, t_0)$  [ $\equiv P(x, t)$  for short] of finding a particle at position  $x$  and time  $t$ , whose initial space-time position is  $x_0$  and  $t_0$ . The 1D Smoluchowski equation for  $P(x, t)$  reads [45]

$$\frac{\partial P(x, t)}{\partial t} = D_0 \frac{\partial^2 P(x, t)}{\partial x^2} + \frac{1}{\xi} \frac{\partial}{\partial x} \left[ P(x, t) \frac{dU(x)}{dx} \right], \quad (3)$$

where  $D_0 = k_B T / \xi$  is the particle's free diffusion coefficient without the influence of  $U(x)$  and  $k_B T$  is the thermal energy of the particle. The two terms on the right side of Eq. (3) are, respectively, the diffusive and convective flux densities of the particle. In the steady state,  $\partial P(x, t) / \partial t = 0$  and Eq. (3) becomes

$$k_B T \frac{d^2 P_{ss}(x)}{dx^2} + \frac{d}{dx} \left[ P_{ss}(x) \frac{dU(x)}{dx} \right] = 0. \quad (4)$$

The steady-state solution  $P_{ss}(x)$  can be obtained analytically for the periodic potential  $U_0(x) = U_0(x + \lambda)$ . We find Eq. (4) admits the following steady-state solution (see Appendix for detailed derivations):

$$P_{ss}(x) = \frac{I_-(x)}{\frac{1}{\lambda} \int_0^\lambda dx I_-(x)}, \quad (5)$$

where

$$I_\pm(x) = \frac{1}{\lambda} \int_0^\lambda dy e^{\pm[U(x) - U(x \mp y)] / k_B T}. \quad (6)$$

With this solution, the flux  $\tilde{J}_{ss}$  along the direction of the external force  $F$  has the form

$$\tilde{J}_{ss} = v_T \frac{1 - e^{-F\lambda/k_B T}}{\frac{1}{\lambda} \int_0^\lambda dx I_-(x)}, \quad (7)$$

where  $v_T = D_0 / \lambda$  is the thermal velocity. In the above,  $\tilde{J}_{ss} = v$  has the dimension of velocity. Equation (7) was obtained previously in Ref. [41]. We now define a dimensionless flux,  $J_{ss} = \tilde{J}_{ss} / v_T = v / v_T$ .

The non-Boltzmann character in Eq. (5) is a result of the NESS with a nonzero flux. Therefore, extra caution must be taken when one attempts to extract the potential  $U(x)$  from the measured  $P_{ss}(x)$ . Simply taking the logarithm of  $P_{ss}(x)$  can correctly give  $U(x)$  only when there is no external force (i.e., zero flux). Instead, the 1D potential  $U(x)$  can be reconstructed from the measured  $P_{ss}(x)$  and  $J_{ss}(x)$  via the equation

$$\frac{U(x) - U(0)}{k_B T} = -\ln \frac{P_{ss}(x)}{P_{ss}(0)} - \frac{J_{ss}}{\lambda} \int_0^x \frac{dy}{P_{ss}(y)}, \quad (8)$$

where  $U(0)$  is the potential at the reference state with  $x = 0$ . The last term on the right-hand side of Eq. (8) measures deviations of the NESS-PDF  $P_{ss}(x)$  from the Boltzmann distribution, which is given by the first term on the right-hand side of Eq. (8). Equation (8) provides a nonlocal (integral) relationship between  $U(x)$  and  $P_{ss}(x)$ . A similar relationship was obtained recently for a driven colloidal particle in a toroidal trap [21] and a 2D rotational fluid under nonconservative forcing [46].

For small values of  $J_{ss}$  or for those values of  $x$  in which  $P_{ss}(x)$  reaches its peak value [i.e., when  $1/P_{ss}(x)$  is small], the second term on the right-hand side of Eq. (8) is a small quantity and the resulting  $P_{ss}(x)$  becomes close to the equilibrium distribution function  $P_B(x)$ . The difference between  $P_{ss}(x)$  and  $P_B(x)$  can be obtained systematically by iterative expansion using  $J_{ss}$  as an expansion parameter. After some algebra, one obtains

$$P_{ss}(x) = P_B(x) [1 - \mu(x)J_{ss} + \nu(x)J_{ss}^2 + \mathcal{O}(J_{ss}^3)], \quad (9)$$

where

$$\mu(x) = q_0(x) - \langle q_0 \rangle_E \quad (10)$$

and

$$\nu(x) = \frac{1}{2} [q_0^2(x) - \langle q_0^2 \rangle_E] - [q_1(x) - \langle q_1 \rangle_E]. \quad (11)$$

In the above,

$$q_0(x) = \int_0^x \frac{dy}{P_B(y)}, \quad (12)$$

$$q_1(x) = \int_0^x dy \frac{q_0(y)}{P_B(y)}, \quad (13)$$

and  $\langle f \rangle_E = \int dx f(x) P_B(x)$  stands for the equilibrium average. It is easy to verify that  $\langle \mu \rangle_E = 0$ ,  $\langle \nu \rangle_E = 0$ , and  $P_{ss}(x)$  in Eq. (9) is normalized.

Our exact steady-state solution in Eq. (5) further allows us to derive an exact expression for the effective friction coefficient  $\xi_{\text{eff}}$ . By putting  $x = \lambda$  in Eq. (8), one has  $F\lambda^2/k_B T = J_{ss} \int_0^\lambda \frac{dx}{P_{ss}(x)}$ . Since  $F = \xi_{\text{eff}} v$ , we have

$$\xi_{\text{eff}}(F) = \frac{\xi}{\lambda^2} \int_0^\lambda \int_0^\lambda \frac{I_-(y)}{I_-(x)} dx dy, \quad (14)$$

where  $\xi$  is the friction coefficient for a flat surface [ $U_0(x) = 0$ ].

## B. Two-dimensional numerical results

In the experiment to be described below, we need to consider 2D motion of the particles, in which no analytical solution for  $P_{ss}(x, y)$  is available at the moment. In this case, we numerically solve the 2D Smoluchowski equation for the time-dependent PDF  $P(x, y; t)$  and obtain the NESS solution  $P_{ss}(x, y) \equiv P(x, y; t \rightarrow \infty)$  when the time  $t$  becomes so long that  $P(x, y; t)$  does not change with  $t$  anymore. To do that, we first construct a 2D potential using the following trial function

$$U_0(x, y) = A \left[ \cos(x) + \cos\left(\frac{\sqrt{3}y}{2} - \frac{x}{2}\right) + \cos\left(-\frac{\sqrt{3}y}{2} - \frac{x}{2}\right) \right], \quad (15)$$

where  $A$  is a tunable amplitude of the potential in units of thermal energy  $k_B T$ . This potential field has periodic peaks of  $3A$  in amplitude and potential wells of  $-1.5A$ , with an energy span of  $4.5A$  between the two extremes. The smallest energy barrier between the two neighboring wells is  $0.5A$ .

Figure 1 shows a 3D plot of the potential  $U_0(x, y)$  generated by Eq. (15) with  $A = 3$  (i.e., the energy barrier between

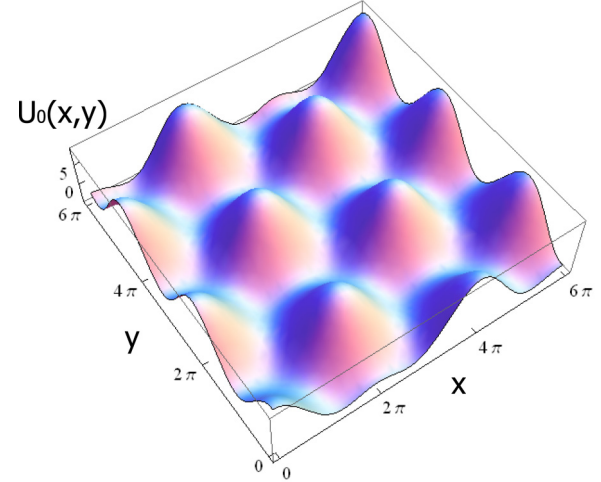


FIG. 1. (Color online) 3D plot of the potential  $U_0(x, y)$  generated by Eq. (15) with  $A = 3$ .

the two neighboring wells is  $1.5 k_B T$ ). Each potential well has three symmetrically placed exits connecting to three identical neighboring wells. The direct connections between the neighboring potential wells make up a honeycomb lattice with the potential wells being the lattice grids. The period of the honeycomb lattice is  $\lambda = 2\pi/\sqrt{3}$ . We now define the force unit associated with the thermal energy  $k_B T$  as  $F_T \equiv k_B T/\lambda$ . Then the tilted potential in Eq. (3) can be written as

$$\frac{U(x)}{k_B T} = \frac{U_0(x)}{k_B T} - \frac{Fx}{F_T \lambda}. \quad (16)$$

It will be shown below that the 2D potential  $U_0(x, y)$  shown in Fig. 1 has the basic structure and symmetry very similar to those of experimentally obtained potential.

Without an external force (i.e.,  $F = 0$ ), the system is at equilibrium and one can use the Boltzmann distribution in Eq. (1) to calculate the equilibrium PDF  $P(x, y)$  for a given potential  $U_0(x, y)$ . Figure 2(a) shows a 2D contour plot of the resulting  $P(x, y)/P_0$  calculated using  $U_0(x, y)$  as shown in Fig. 1. Here  $P(x, y)/P_0$  is normalized with  $P_0$  being the peak value of  $P(x, y)$  located at the potential well. The threefold symmetry of the bright triangular areas with  $P(x, y)/P_0 > 0.5$  is a consequence of the structure of the underlying potential wells in Fig. 1; each peak in  $P(x, y)$  has three identical exits to the three nearest-neighboring peaks. The areas with relatively small probability, i.e.,  $P(x, y)/P_0 < 0.1$ , are marked as dark blue, which correspond to the “mountain” regions in Fig. 1. Note that the value of  $A$  in Eq. (15) does not change the qualitative observations described here.

When an external force  $F$  is applied to the system, the Boltzmann distribution is no longer valid. The solution  $P(x, y, t)$  of the 2D Smoluchowski equation will change with  $t$  until it gradually relaxes to the NESS solution  $P_{ss}(x, y)$  after a certain period  $\tau$ , which depends on the amplitude of  $F$ . The relaxation time  $\tau$  is shortened if a larger external force  $F$  is used. This is because with increasing  $F$ , the effective energy barrier is reduced and so does the mean first passage time [40,47]. We numerically solve the 2D version of Eq. (3) for

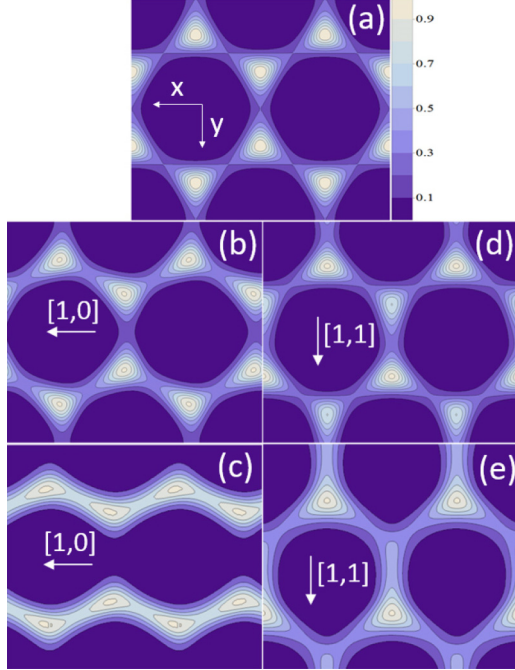


FIG. 2. (Color online) (a) 2D contour plot of equilibrium PDF  $P(x,y)/P_0$  for the potential  $U_0(x,y)$  shown in Fig. 1. [(b) and (c)] Evolution of the NESS-PDF  $P_{ss}(x,y)/P_0$  with increasing values of  $F$  along the  $[1,0]$  direction with (b)  $F/F_T = 1.5$  and (c)  $F/F_T = 5.0$ . [(d) and (e)] Evolution of  $P_{ss}(x,y)/P_0$  with increasing values of  $F$  along the  $[1,1]$  direction with (d)  $F/F_T = 1.5$  and (e)  $F/F_T = 5.0$ . The arrows indicate the  $[1,0]$  and  $[1,1]$  crystalline directions.

$P(x,y,t)$  with the following initial and boundary conditions:

$$\begin{aligned} P(x,y,0) &= e^{-U_0(x,y)/k_B T}, \\ P(0,y,t) &= P(2m\pi, y, t), \\ P(x,0,t) &= P(x, 2m\pi/\sqrt{3}, t), \end{aligned} \quad (17)$$

with  $m = \pm 1, \pm 2, \dots$ . In the calculation, we set the values of  $D_0$  and  $\xi$  in the 2D Smoluchowski equation equal to unity for convenience. The NESS-PDF  $P_{ss}(x,y)$  is effectively obtained by solving  $P(x,y,t)$  at  $t = 10$ , which is much longer than the relaxation time  $\tau$  needed for all the forces in use. For example, we find  $\tau \simeq 2$  when the external force  $F/F_T$  is unity.

In Figs. 2(b)–2(e) we indicate the two orthogonal directions of forcing labeled as  $[1,0]$  and  $[1,1]$  with an arrow, which coincide with the two primary directions of the bottom crystalline pattern. Figures 2(b) and 2(c) show the evolution of the numerically calculated  $P_{ss}(x,y)/P_0$  with increasing values of  $F$  along the  $[1,0]$  direction. The PDFs around the potential wells can be categorized into two characteristic shapes, the downward triangles (“ $\nabla$ ” regions) and upright triangles (“ $\Delta$ ” regions). At equilibrium, they are equivalent with each other under reflection about the midheight plane shown in Fig. 2(a). The threefold symmetry observed for the equilibrium PDF is broken even at a very small force  $F/F_T = 1.5$ , as shown in Fig. 2(b). Under larger forces, e.g.,  $F/F_T = 5$  in Fig. 2(c), the NESS-PDF is transformed into parallel zigzag bands, and the probability distribution across the lateral direction (relative to the forcing direction) between different bands is greatly

suppressed. Another feature found in Fig. 2(c) is that the peak positions of the NESS-PDF  $P_{ss}(x,y)$  are shifted laterally in the direction of the external force, deviating from the center of the original potential wells. Figures 2(b) and 2(c) thus suggest that particles in the tilted potential tend to occupy more frequently the longitudinal zigzag bands compared with the equilibrium distribution. The suppression of the probability in the lateral direction between the neighboring potential wells from different bands are reduced by the external force along the  $[1,0]$  direction.

Figures 2(d) and 2(e) show the evolution of the calculated  $P_{ss}(x,y)/P_0$  with increasing values of  $F$  along the  $[1,1]$  direction. In this case, the external force also breaks the threefold symmetry of the NESS-PDF around the potential wells in a way that differs substantially from that under the forcing along the  $[1,0]$  direction. The probability distribution in the  $\nabla$ -shaped regions is shrunk, whereas in the  $\Delta$ -shaped regions the probability distribution is expanded. In other words, unlike the  $[1,0]$  forcing which maintains the symmetry of reflection between the  $\nabla$  and  $\Delta$  regions, the  $[1,1]$  forcing breaks this symmetry and changes the geometric shape of the two characteristic regions. As the force is further increased to  $F/F_T = 5$ , the peaks of the resulting NESS-PDF  $P_{ss}(x,y)$  in the  $\nabla$ -shaped regions gradually disappear or merge to the  $\Delta$ -shaped regions. In this case, one cannot tell if there is any energy barrier located near the enlarged  $\nabla$  regions. Another unique feature associated with the  $[1,1]$  forcing is that because the “sea level” of the NESS-PDF keeps rising, the high-energy “islands” (low-probability regions marked in dark blue) are gradually submerged and their size keeps shrinking with increasing  $F$ . In other words, the  $[1,1]$  forcing makes it easier for particles to occupy the high-energy regions that are otherwise difficult to reach.

The numerical results shown in Fig. 2 thus reveal that the external force  $F$  can significantly change the actual potential explored by the particles by either reducing or increasing the probability of visiting particular regions depending on both the force amplitude and direction. In the experiment to be described below, we measure the NESS-PDF  $P_{ss}(x,y)$  as a function of  $F$  with different amplitudes and directions. The experimental results will be compared with the qualitative observations discussed above. We will also examine the validity of the analytical solutions shown in Eqs. (5) and (8) with the measured quasi-1D potential  $U_0(x)$  and  $P_{ss}(x)$ .

### III. EXPERIMENT

Details about the apparatus and the experimental method have been described elsewhere [19,40], and here we mention only some key points.

#### A. Apparatus and sample preparation

Figure 3 shows the sample cell used in the experiment, which is tilted at an angle  $\theta$  with respect to the vertical (gravity) direction. The entire sample cell has two fluid chambers; the central hole is used to hold the colloidal sample and the outer surrounding chamber contains additional solvent (water with the same salt concentration) to prevent sample evaporation. It is placed on the stage of an inverted microscope (Leica

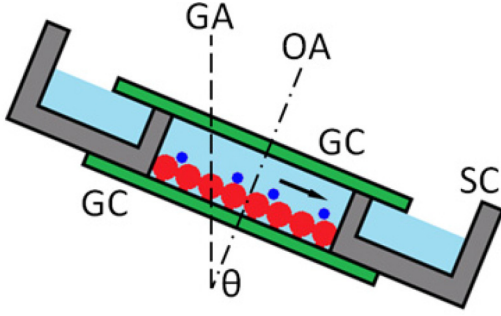


FIG. 3. (Color online) Schematic diagram of the sample cell (side view): SC, stainless steel cell; GC, glass cover slip; GA, gravity axis; OA, optical axis;  $\theta$ , tilt angle of the sample cell; red particles, large silica spheres forming a monolayer crystal on the bottom glass substrate; blue particles, smaller diffusing particles on top of the colloidal crystal; arrow, direction of the force  $F$  acting on the diffusing particles.

DM-IRB), and the motion of the particles is viewed from below using bright-field microscopy. Movies of particle motion are recorded using a monochrome CCD camera (CoolSNAP, Media Cybernetics) and streamed to the hard drive of a host computer. They are taken at 7 frames per second. A commercial image acquisition software (ImagePro, Media Cybernetics) is used to control the camera. The recorded images have a spatial resolution of  $1392 \times 1040$  pixels and 256 gray scales.

Plain silica spheres of different sizes are used in the experiment and they are purchased from Bangs Laboratories. All the purchased samples are thoroughly washed using deionized water by repeated centrifugation. Typically, we repeat the centrifugation procedures for 8–10 times to make sure that all the impurities in the solution are removed. The final solution is found to contain only monodisperse silica spheres. To prepare a close-packed monolayer of colloidal spheres near the bottom glass substrate, we add the colloidal solution into the sample cell one drop ( $\sim 200 \mu\text{L}$ ) at a time until the area fraction  $n$  occupied by the silica spheres in the bottom layer reaches  $n \simeq 0.7$ . Then a 1-mL syringe is used to continue the process with a smaller drop ( $10\text{--}20 \mu\text{L}$ ) of the particle solution added at a time until  $n$  approaches the packing limit  $n_c \simeq 0.8$ . The sample is then left open for complete evaporation of water in the solution and the remaining particles are attached to the glass substrate by van de Waals forces.

During evaporation, the silica spheres self-assemble into a monolayer of close-packed crystal patches. Then we fill the sample cell with a 0.1 mM aqueous solution of NaCl followed by the addition of a drop of silica suspension into the salt solution using a 1-mL syringe. After several minutes, the silica spheres settle down on top of the bottom colloidal crystal layer, and the particle number in the view area is counted using ImagePro. This procedure is repeated until a desired area fraction  $n$  for the second layer particles is reached. The sample cell is then covered with a glass cover slip to prevent solvent evaporation. Two colloidal samples, S1 and S2, with two different pairs of top and bottom particles, are used in the experiment and their properties are given in Table I. These two samples were also used in a recent study of the

TABLE I. Two colloidal samples used in the experiment with different pairs of top and bottom particles and the obtained external potential parameters, including lattice constant  $\lambda$ , energy barrier height  $E_b/k_B T$ , critical force  $F_c/F_T$ , and  $R \equiv \langle \exp[U_0(x)/k_B T] \rangle_\lambda \langle \exp[-U_0(x)/k_B T] \rangle_\lambda$  [40].

| Samples | Top/bottom ( $\mu\text{m}$ ) | $\lambda$ ( $\mu\text{m}$ ) | $E_b/k_B T$ | $F_c/F_T$    | R    |
|---------|------------------------------|-----------------------------|-------------|--------------|------|
| S1      | 2.1/2.9                      | 1.7                         | 1.5         | $5.9 \pm 2$  | 1.3  |
| S2      | 3.6/3.6                      | 2.1                         | 6.7         | $22.8 \pm 2$ | 40.0 |

dynamics of individual particles in the tilted periodic potential [40].

### B. Video microscopy and image analysis

Figure 4 shows the silica spheres of diameter  $d = 3.6 \mu\text{m}$  (bright spots with a nonuniform intensity profile) diffusing over the bottom colloidal crystal layer (honeycomb lattice) made of the same silica spheres (sample S2). The image is taken with the focal plane located between the two layers of silica spheres so the out-of-focus image of the bottom colloidal crystal becomes a honeycomb lattice and the top diffusing particles appear as bright spots. The nonuniform intensity profile of the diffusing particles is caused by the interference with the bottom-layer particles. The white arrows indicate the  $[1,0]$  and  $[1,1]$  crystalline directions of the bottom crystal layer.

The microscope is placed on a homemade incline with an adjustable tilt angle  $\theta$  up to  $35^\circ$  with respect to the horizontal base. With this setup the external force  $F$  acting on the top-layer diffusing particles is provided by gravity,

$$F = \Delta m g \sin(\theta), \quad (18)$$

where  $\Delta m$  is the buoyant mass of the diffusing particles and  $g$  is the gravitational acceleration. Because  $\Delta m$  scales with  $d^3$ , the force  $F$  is strongly dependent on the particle size. For sample S1, we find  $F \simeq (0.04 \text{ pN}) \sin(\theta)$ , and the largest force that can be achieved for  $\theta = 30^\circ$  is about 0.02 pN or  $8.2 F_T$ . For sample S2, we have  $F \simeq (0.2 \text{ pN}) \sin(\theta)$ , so a larger force

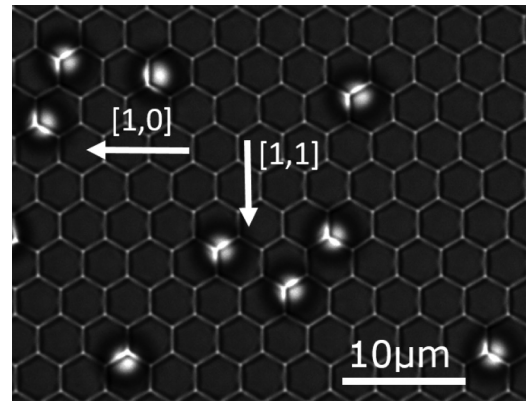


FIG. 4. Microscope image of sample S2. The uniform honeycomb pattern in the background is the optical pattern resulting from the bottom layer colloidal crystal. The bright dots with a nonuniform intensity profile are the diffusing particles in the top layer. The arrows indicate the  $[1,0]$  and  $[1,1]$  crystalline directions. The scale bar is  $10 \mu\text{m}$ .

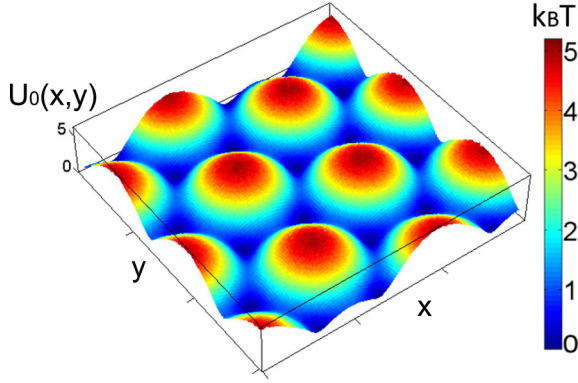


FIG. 5. (Color online) Three-dimensional plot of the measured potential  $U_0(x, y)$  for sample S1 at equilibrium. The plotted area of  $U_0(x, y)$  is  $7.3 \times 7.5 \mu\text{m}^2$ .

up to  $\sim 0.1$  pN or  $41F_T$  can be achieved. Experimentally,  $F$  is determined via the equation  $F = \xi v_0$ , where the values of the friction coefficient  $\xi = k_B T/D_0$  and drift velocity  $v_0$  are obtained from the simultaneous measurements of the particle's diffusion coefficient  $D_0$  and drift velocity  $v_0$  over a flat incline at various tilt angles  $\theta$ . In this way,  $F$  is uniquely determined without any adjustable parameter. A detailed description of the experimental procedure can be found in Ref. [40].

By applying a standard Gaussian image filter from the MATLAB image processing toolbox, we can recover the uniform Gaussian-like intensity profile for each diffusing particle. The central position of the intensity profile is thus chosen as the center of the diffusing particle. With this method we are able to obtain a repeatable tracking accuracy of  $\sim 1$  pixel, which is 74 nm. A homemade MATLAB program based on the standard tracking algorithm [18] is used to track the trajectory of the diffusing particles from consecutive images.

## IV. RESULTS AND DISCUSSIONS

### A. Periodic potential of untilted samples

When the sample is leveled, the corrugated surface of the bottom colloidal crystal layer provides a gravitational potential field for the diffusing particles on the top layer. In the experiment, we use the method described in Ref. [19] to measure the potential  $U_0(x, y)$  of the two colloidal samples. The occupation statistics of the diffusing particles on the top layer is obtained by adding together  $10^5$  images, each containing  $\sim 100$  particles, and counting the number of particles in each pixel. In doing so, we obtain the population probability histogram (pph)  $P_l(x, y)$  of finding a diffusing particle at location  $(x, y)$ , which is related to the (gravitational) potential  $U_0(x, y)$  via the Boltzmann distribution, as shown in Eq. (1). All the measurements are made at the area fraction  $n \simeq 0.15$ . At this area fraction, the interaction between the diffusing particles is negligibly small and Eq. (1) is valid.

Figure 5 shows a 3D plot of the measured potential  $U_0(x, y)$  for sample S1. The minimum energy at the bottom of the potential wells (dark blue) is set to be zero. The threefold symmetry of the external potential around the potential wells can be clearly seen. The maximum energy on the top of the particles (red) is  $\sim 5.2k_B T$ . The smallest energy barrier

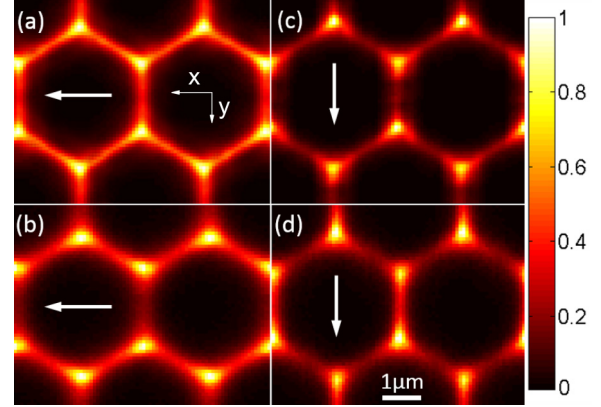


FIG. 6. (Color online) [(a) and (b)] Evolution of the measured NESS-PDF  $P_{ss}(x, y)/P_0$  for sample S1 with increasing values of  $F$  along the  $[1,0]$  direction with (a)  $F/F_T = 1.4$  ( $\theta = 5.5^\circ$ ) and (b)  $F/F_T = 5.2$  ( $\theta = 20^\circ$ ). [(c) and (d)] Evolution of the measured NESS-PDF  $P_{ss}(x, y)/P_0$  with increasing values of  $F$  along the  $[1,1]$  direction with (c)  $F/F_T = 1.4$  and (d)  $F/F_T = 5.2$ . The value of  $P_0$  is chosen so  $P_{ss}(x, y)/P_0 = 1$  at the peak positions. The arrows indicate the forcing directions. The scale bar is  $1 \mu\text{m}$ .

between the two neighboring potential wells is  $E_b \simeq 1.5k_B T$ , which is very close to that shown in Fig. 1. Because the bottom layer is periodic, the measured  $U_0(x, y)$  can be divided into repetitive cells, each containing two nearby potential wells together with a connecting barrier. We then sum up the values of  $U_0(x, y)$  from different cells with correct symmetry and generate the single-cell potential with a higher statistical accuracy. In Ref. [19], we have demonstrated that the 2D pph  $P_l(x, y)$  can be converted into a 1D pph  $P_{l_s}(X)$ , where  $X$  is the coordinate along the line connecting the two peaks of  $P_l(x, y)$ . Similarly, the 2D potential  $U_0(x, y)$  can also be projected into a 1D plot  $U_0(X)$ , which will be presented below.

### B. 2D steady-state distributions $P_{ss}(x, y)$ over a tilted periodic potential

#### 1. $P_{ss}(x, y)$ for sample S1

Figures 6(a) and 6(b) show the evolution of the measured NESS-PDF  $P_{ss}(x, y)/P_0$  with increasing values of  $F$  along the  $[1,0]$  direction. The averaging scheme over the repetitive cells, as described in the above, is used here. Results obtained at two tilt angles,  $\theta = 5.5^\circ$  and  $\theta = 20^\circ$ , corresponding to  $F/F_T \simeq 1.4$  and  $F/F_T \simeq 5.2$ , respectively, are presented. Compared to the equilibrium  $P(x, y)/P_0$ , which has the threefold symmetry as shown in Fig. 2(a), the shape of the measured  $P_{ss}(x, y)/P_0$  in the peak region is stretched to the left and is elongated along the zigzag path. The probability distribution across the energy barriers perpendicular to the  $[1,0]$  orientation gradually decreases with increasing  $F$  to a small but nonzero value. This behavior qualitatively agrees with the numerical results as shown in Fig. 2 for small values of  $F/F_T$ .

Figures 6(c) and 6(d) show the evolution of the measured  $P_{ss}(x, y)/P_0$  with increasing values of  $F$  along the  $[1,1]$  direction. The probability distribution contains two sets of identical regions; one set of regions are the  $\Delta$ -shaped regions located near the upper border of the figures and the other set of

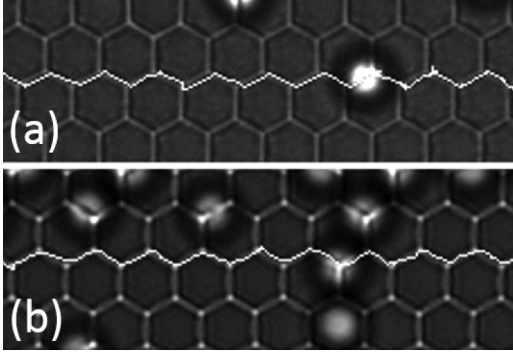


FIG. 7. Measured trajectories (white curves) of a top-layer particle for sample S2 under the influence of a gravitational pulling force  $F$  along the  $[1,0]$  direction toward the left. The amplitude of  $F$  is (a)  $F/F_T = 22.5$  ( $\theta = 14^\circ$ ) and (b)  $F/F_T = 46.8$  ( $\theta = 31^\circ$ ).

regions are the  $\nabla$ -shaped regions below the  $\Delta$ -shaped regions. It is seen that the size of the  $\Delta$ -shaped regions increases with the force  $F$ , whereas the size of the  $\nabla$ -shaped regions shrinks with increasing  $F$ . This behavior qualitatively agrees with the numerical results as shown in Fig. 2.

## 2. $P_{ss}(x, y)$ for sample S2

Figure 7 shows the measured trajectories (white curves) of a top-layer particle for sample S2 under the influence of a gravitational pulling force  $F$  along the  $[1,0]$  direction toward the left. Also shown is the bottom colloidal crystal pattern, which serves as a visual guide of the underlying potential. It is seen that the particle actually follows a zigzag path, which has a lower energy barrier. As a result, only a fraction of the gravitational pulling force,  $F = \Delta mg \sin(\theta) \cos(\pi/6)$ , is applied along the particle's path. After this correction, the effective quasi-1D pulling force in Fig. 7(a) is  $F/F_T = 22.5$  (for the tilt angle  $\theta = 14^\circ$ ) and that in Fig. 7(b) is  $F/F_T = 46.8$  (for the tilt angle  $\theta = 31^\circ$ ).

For a given quasi-1D potential  $U_0(X)$ , there exists a critical force  $F_c$ , which is given by the positive root of  $F_c = U_0'(X_c)$ , where  $X_c$  is the inflection point of  $U_0(X)$  given by  $U_0''(X_c) = 0$ . At the critical force  $F_c$ , the effective barrier vanishes [48,49]. The values of  $F_c/F_T$  for the two colloidal samples used are given in Table I. When  $F \gg F_c$ , the particle flux density  $J_{ss}$  (or drift velocity  $v$ ) becomes the same as that over an incline without an energy barrier [40]. It can be shown that the effective friction coefficient  $\xi_{\text{eff}}(F)$  in Eq. (14) decays quickly with  $F$ , and  $\xi_{\text{eff}} \simeq \xi$  for  $F \gg F_c$ , as expected.

While the amplitude of  $F$  is varied by a factor of 2, the trajectories shown in Figs. 7(a) and 7(b) retain some common features as follows. (i) Over a long distance ( $\gg \lambda$ ), the particle drifts from the right to the left, following the direction of  $F$ . For smaller distances ( $< \lambda$ ), however, the particle spends more time diffusing within a potential well. The mean drift velocity of the particle is thus caused by the breakdown of the detailed balance between the forward barrier hopping and backward barrier hopping. As a result, the mean velocity  $v$  of the particle is physically meaningful only when the particle's traveling distance becomes longer than  $\lambda$ . (ii) Lateral or backward hopping against the gravitational

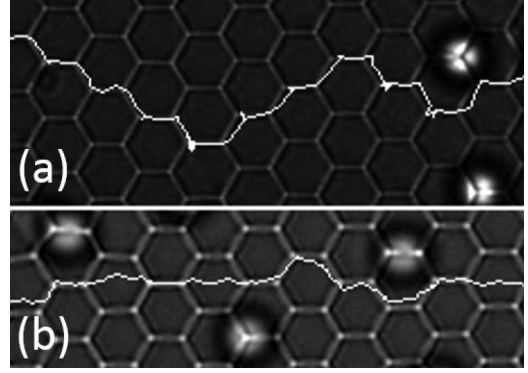


FIG. 8. Measured trajectories (white curves) of a top-layer particle for sample S2 under the influence of a gravitational pulling force  $F$  along the  $[1,1]$  direction toward the left. The amplitude of  $F$  is (a)  $F/F_T = 22.5$  ( $\theta = 14^\circ$ ) and (b)  $F/F_T = 46.8$  ( $\theta = 31^\circ$ ).

pulling force is rarely observed. (iii) The particle's trajectory follows the straight zigzag path guided by the underlying low-energy path connecting the adjacent potential wells. (iv) The particle's trajectories are centered around the quasi-1D transition paths without much spreading. From the measured particle trajectories, we calculate the lateral shift of the particles away from their equilibrium position at the potential minimum due to the external force and find that this lateral shift is less than 1 pixel ( $=70$  nm) in our experiment. This accounts for an error of less than 4% compared with one half of the lattice constant ( $\lambda/2 = 1.8 \mu\text{m}$ ).

Figure 8 shows the situation for sample S2 when the direction of  $F$  is changed to the  $[1,1]$  orientation of the bottom crystal. In this case, the transition paths on the honeycomb lattice can be categorized into two groups based on their orientations relative to the direction of  $F$ . One group of transition paths are parallel to  $F$  ( $\parallel$  path) and the other group has a  $\pm\pi/3$  incline angle with respect to the direction of  $F$  ( $\pi/3$  path). It is seen from Fig. 8(a) that at  $F/F_T = 22.5$  (tilt angle  $\theta = 14^\circ$ ), the particle follows a quasi-1D path with an alternating  $\parallel$  path followed by a  $\pm\pi/3$  path. At each bifurcation point, the particle has an equal probability to go either along the  $+\pi/3$  path or along the  $-\pi/3$  path. In this way, the particle explores a quasi-1D potential on the colloidal lattice. At a larger force  $F/F_T = 46.8$  (tilt angle  $\theta = 31^\circ$ ), however, the particle can occasionally jump over the top of the bottom-layer sphere located at the bifurcation point, an event which seldom occurs for the leveled sample S2. This observation provides an experimental support to the numerical results discussed in Sec. II B that increasing  $F$  in the  $[1,1]$  direction makes the high-energy region more accessible to the particles. Figure 8 thus demonstrates that the actual regions inside the potential  $U_0(x, y)$  being explored by the particle is strongly influenced by the external force  $F$  along the  $[1,1]$  direction. This effect is very weak, if not completely negligible, when  $F$  is along the  $[1,0]$  direction.

The above characteristic features of the particle trajectory are also reflected in the measured NESS-PDF  $P_{ss}(x, y)/P_0$ . Figures 9(a) and 9(b) shows the measured  $P_{ss}(x, y)/P_0$  at two different values of the applied force along the  $[1,0]$  direction. In contrast to the equilibrium  $P(x, y)/P_0$  as shown in Fig. 2(a), the

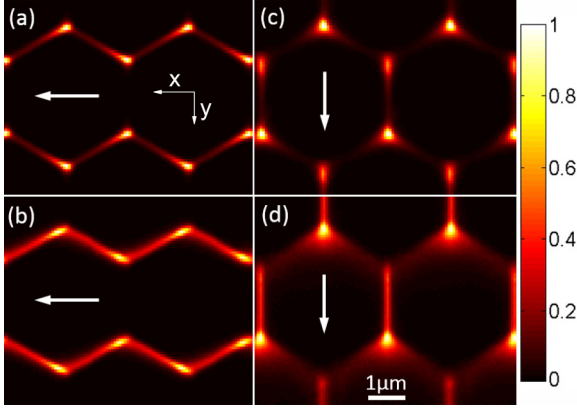


FIG. 9. (Color online) [(a) and (b)] Evolution of the measured NESS-PDF  $P_{ss}(x,y)/P_0$  for sample S2 with increasing values of  $F$  along the  $[1,0]$  direction with (a)  $F/F_T = 22.5$  ( $\theta = 14^\circ$ ) and (b)  $F/F_T = 46.8$  ( $\theta = 31^\circ$ ). [(c) and (d)] Evolution of the measured  $P_{ss}(x,y)/P_0$  with increasing values of  $F$  along the  $[1,1]$  direction with (c)  $F/F_T = 22.5$  and (d)  $F/F_T = 46.8$ . The value of  $P_0$  is chosen so that  $P_{ss}(x,y)/P_0 = 1$  at the peak positions. The arrows indicate the forcing directions. The scale bar is  $1 \mu\text{m}$ .

measured  $P_{ss}(x,y)/P_0$  does not share the threefold symmetry that the equilibrium  $P(x,y)/P_0$  has. Instead, the shape of  $P_{ss}(x,y)/P_0$  in the peak region is clearly stretched to the left and is elongated along the zigzag path. The probability distribution across the energy barriers perpendicular to the  $[1,0]$  orientation quickly vanishes with increasing  $F$ . This effect is consistent with the individual particle's trajectories as shown in Fig. 7. Along the quasi-1D zigzag path, the peak position of the measured  $P_{ss}(x,y)$  is no longer located at the center of the potential wells of  $U_0(x,y)$ . Rather, it is shifted several pixels to the left. Furthermore, the zigzag paths are centered on the quasi-1D lattice without much spreading. For the  $[1,0]$ -orientation forcing, the high-energy regions of  $U_0(x,y)$  are still not available to the particles, and thus their motion remains quasi-1D. We will examine the functional form of the measured  $P_{ss}(x,y)$  in the next section.

Figures 9(c) and 9(d) shows the measured  $P_{ss}(x,y)/P_0$  at two different values of the applied force  $F$  along the  $[1,1]$  direction. As  $F$  increases, the size of the  $\Delta$ -shaped regions (near the upper border of the figures) gradually grows and extends downward to the high-energy regions. This finding is also consistent with the observed particle's trajectories as shown in Fig. 8. Thus the potential being explored by the particles in the  $[1,1]$ -orientation forcing cannot be approximated by a quasi-1D lattice anymore. Instead, the system becomes increasingly 2D as the gravitational pulling force increases. The probability peaks in the  $\nabla$ -shaped regions, on the other hand, seem to vanish with increasing  $F$ . From Fig. 9(d), one can hardly tell if there is a peak in the  $\nabla$ -shaped region from its surroundings. The measured  $P_{ss}(x,y)/P_0$  along the  $\parallel$  path merges into the  $\Delta$  regions.

The measured  $P_{ss}(x,y)/P_0$  for samples S1 and S2 show the same qualitative features as the numerical results as shown in Fig. 2. Our observations reveal that forcing in the  $[1,0]$  crystal orientation can separate  $P_{ss}(x,y)/P_0$  into parallel zigzag bands while keeping the particles to explore an effective

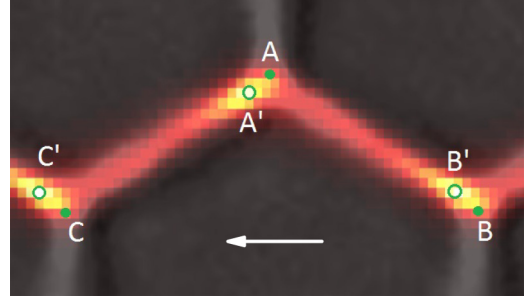


FIG. 10. (Color online) Superposition of the background image of the bottom colloidal crystal layer (black and white) and 2D plot of the measured  $P_{ss}(x,y)$  (red) with brighter regions indicating higher values of  $P_{ss}(x,y)$ . Positions  $A$ ,  $B$ , and  $C$  (green dots) indicate the locations of the potential wells in  $U_0(x,y)$ . Positions  $A'$ ,  $B'$ , and  $C'$  (green circles) indicate the peak positions of the measured  $P_{ss}(x,y)$ . The arrow indicates the direction of the force  $F$  along the  $[1,0]$  orientation.

quasi-1D potential. Forcing in the  $[1,1]$  orientation, however, redistributes  $P_{ss}(x,y)/P_0$  into high-energy regions and thus alters the potential actually being explored by the particles. In the next section, we focus on the NESS-PDF measurements with  $F$  being aligned along the  $[1,0]$  crystal orientation and compare the experimental results with the 1D theory given in Sec. II A.

### C. Reconstruction of the potential $U_0(X)$ from the measured $P_{ss}(X)$

We now discuss how to obtain the quasi-1D potential  $U_0(X)$  from the measured  $P_{ss}(x,y)$  for the tilted samples with  $F$  being aligned along the  $[1,0]$  crystal orientation. As shown in Figs. 9(a) and 9(b), the measured  $P_{ss}(x,y)$  in this case has a zigzag shape lying over a quasi-1D lattice. Figure 10 shows a superposition image of the background optical pattern of the bottom colloidal crystal layer and 2D plot of the measured  $P_{ss}(x,y)$  with brighter regions indicating higher values of  $P_{ss}(x,y)$ . The background image of the bottom colloidal crystal layer shows the positions  $A$ ,  $B$ , and  $C$  (green dots) of the potential wells in  $U_0(x,y)$ . They are also the peak positions of the measured equilibrium PDF  $P_{Is}(x,y)$  from the untilted samples. Positions  $A'$ ,  $B'$ , and  $C'$  (green circles) indicate the peak positions of the measured  $P_{ss}(x,y)$ . They are shifted forward along the zigzag path by the external force  $F$  aligned in the  $[1,0]$  orientation. Note that positions  $A'$  and  $B'$  in Fig. 10 sit right on the lines  $\overline{AC}$  and  $\overline{BA}$ , which connect the potential wells of  $U_0(x,y)$ , indicating that the particle trajectories under the  $[1,0]$ -orientation forcing follow the zigzag path without noticeable deviations. Therefore, the effective potential explored by the particles is essentially quasi-1D [19]. Presumably, the new peak positions are determined by a balance between the side push from the force  $F$  in the  $[1,0]$  direction and the restoring force resulting from the equilibrium potential  $U_0(x,y)$ .

In Fig. 11 we show how to determine the position  $A$  of the potential well in  $U_0(x,y)$ . First, two red lines are drawn through the peak positions  $A'$  and  $B'$ . The two lines have a tilted angle of  $5\pi/6$  and  $\pi/6$ , respectively, with respect to the  $[1,0]$

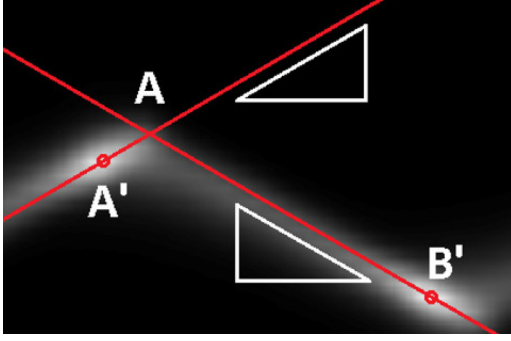


FIG. 11. (Color online) 2D plot of the averaged  $P_{ss}(x,y)$  over the repeated unit cells with brighter regions indicating higher values of  $P_{ss}(x,y)$ . Positions  $A'$  and  $B'$  indicate the peak positions of the measured  $P_{ss}(x,y)$ . The red line  $\overline{AB'}$  has a tilt angle of  $\pi/6$  with respect to the  $[1,0]$  crystal orientation, as illustrated by the lower triangle. The red line  $\overline{AA'}$  has a tilt angle of  $5\pi/6$  with respect to the  $[1,0]$  orientation, as illustrated by the upper triangle. The intersection point  $A$  indicates the position of the potential well in  $U_0(x,y)$ .

crystal orientation. These two tilt angles ensure that positions  $A'$  and  $B'$  are on the quasi-1D transition paths between the potential wells. As shown in Fig. 10, the intersection point  $A$  thus indicates the center of the hidden potential well. The position  $A$  is then taken as the origin of the axis  $X$  along the transition path  $\overline{AB'}$ , from which we obtain the 1D NESS-PDF  $P_{ss}(X)$  from the measured values of  $P_{ss}(x,y)$ . Similarly, the position  $B$  of the other potential well (see Fig. 10) is obtained by making the length  $\overline{AB}$  to be the same as  $\lambda$ . Due to the symmetry, the obtained  $P_{ss}(X)$  along the path  $\overline{AB}$  is the same as that along the path  $\overline{AC}$ .

Figure 12(a) shows the measured 1D equilibrium PDF  $P_{ls}(X)$  as a function of the normalized transition path  $X/\lambda$  (red squares), where  $\lambda$  is the distance between two neighboring potential wells. The data are obtained in the untilted sample S2 ( $F = 0$ ). The values of  $P_{ls}(X)$  are normalized so the summation of  $P_{ls}(X)dX$  over one period is equal to unity. The black solid line is a smooth-fitting curve representing the measured  $P_{ls}(X)$ , from which one obtains the quasi-1D potential  $U_0(X)/k_B T = -\ln[P_{ls}(X)]$ .

Figures 12(b)–12(d) show the evolution of the measured one-dimensional NESS-PDF  $P_{ss}(X)$  (solid symbols) for the tilted sample S2 with increasing values of  $F$  along the  $[1,0]$  direction from  $F/F_T = 22.5$  to  $F/F_T = 46.8$ . The same normalization procedure as described in the above is also applied to the measured  $P_{ss}(X)$  here. The solid lines in Figs. 12(b)–12(d) are the numerically calculated  $P_{ss}(X)$  using Eq. (5) together with the measured  $U_0(X)$  from Fig. 12(a). An excellent agreement between the experiment and numerical calculation is found, further confirming that Eq. (5) and the quasi-1D approach described above are accurate for the experiment.

To obtain the total potential  $U(X)$  via Eq. (8), one needs to measure both the flux density  $J_{ss}$  (or drift velocity  $v$ ) and  $P_{ss}(X)$ . For an  $N$ -step particle trajectory  $(x_1, x_2, \dots, x_N)$ , the drift velocity along the  $x$  axis can be obtained by the equation

$$v_x = \frac{x_N - x_1}{(N - 1)\Delta t}, \quad (19)$$

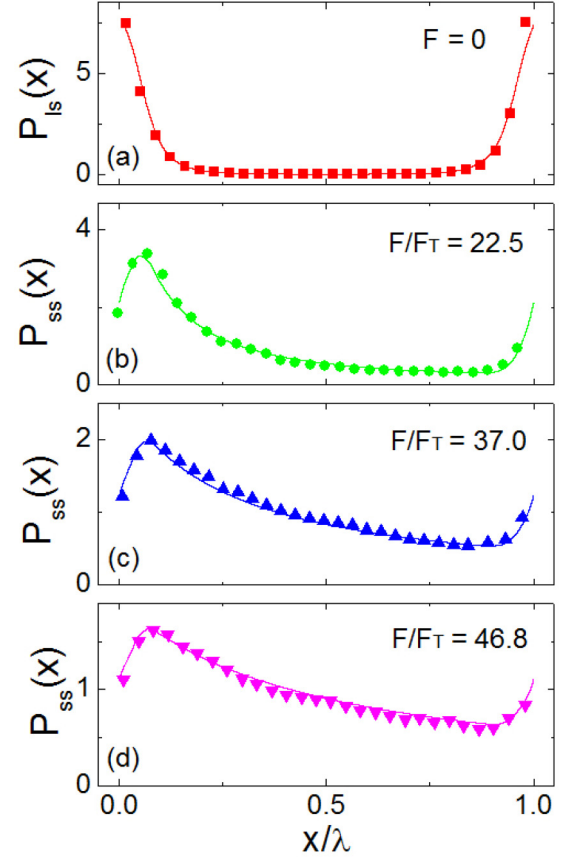


FIG. 12. (Color online) (a) Measured one-dimensional equilibrium PDF  $P_{ls}(X)$  as a function of the normalized transition path  $X/\lambda$  (red squares). The solid line is a smooth-fitting curve representing the measured  $P_{ls}(X)$ . [(b)–(d)] Evolution of the measured one-dimensional NESS-PDF  $P_{ss}(X)$  (solid symbols) with increasing values of  $F$  along the  $[1,0]$  direction with (b)  $F/F_T = 22.5$ , (c)  $F/F_T = 37.0$ , and (d)  $F/F_T = 46.8$ . The solid lines are the numerical results obtained using Eq. (5) together with the measured quasi-1D potential  $U_0(X)/k_B T = -\ln[P_{ls}(X)]$  from (a).

where  $\Delta t$  is the lag time between consecutive frames. For the particles moving along the quasi-1D zigzag paths, the actual drift velocity along the 1D potential is  $v = v_x / \cos(\pi/6)$ . The normalized flux density at the three values of  $F$  in Figs. 12(b)–12(d) is found to be  $J_{ss} = 11 \pm 3$ ,  $28 \pm 4$ , and  $43 \pm 5$ , respectively. With the measured  $P_{ss}(X)$  and  $J_{ss}$ , one can numerically calculate  $U(X)$  using Eq. (8) and then reconstruct the intrinsic potential,  $U_0(X) = U(X) + FX$ , by removing the contribution of the external force  $F$  from  $U(X)$ .

Figure 13 shows the reconstructed 1D potential  $U_0(X)$  from the measured  $P_{ss}(X)$  and  $J_{ss}$  with increasing values of  $F$  along the  $[1,0]$  direction. Because  $U_0(X)$  involves the normal component of the gravity,  $F_n = \Delta mg \cos(\theta)$ , it changes slightly with the tilt angle  $\theta$ . All of the data points in Fig. 13 are divided by a common factor  $\cos(\theta)$  to compensate the reduced gravity effect. Once this correction is applied, all of the data points collapse onto a common master curve. The black solid line is the directly measured  $U_0(X)/k_B T = -\ln[P_{ls}(X)]$  from Fig. 12(a). It is seen that the reconstructed data from the measured  $P_{ss}(X)$  and  $J_{ss}$  agree well with the

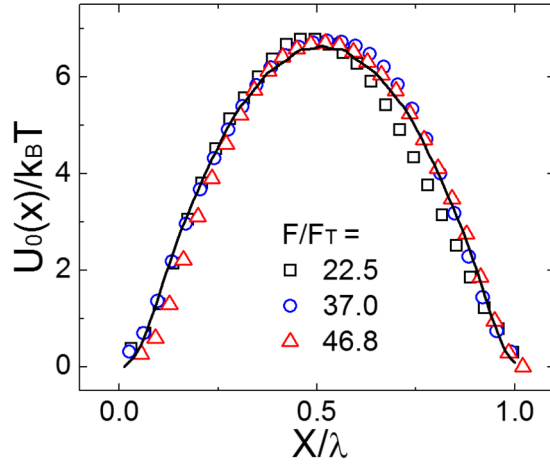


FIG. 13. (Color online) Reconstructed 1D potential  $U_0(X)$  from the measured  $P_{ss}(X)$  and  $J_{ss}$  using Eq. (8). The symbols are obtained with increasing values of  $F$  along the  $[1,0]$  direction for  $F/F_T = 22.5$  (black squares), 37.0 (blue circles), and 46.8 (red triangles). The black solid line is the directly measured  $U_0(X)/k_B T = -\ln[P_{1s}(X)]$  from Fig. 12(a).

directly measured  $U_0(X)/k_B T$  from the equilibrium PDF  $P_{1s}(X)$ . Figure 13 thus verifies the validity of Eq. (8).

A similar attempt was also made in a previous study of NESS dynamics of colloidal particles in a 1D optical trap (optical tweezers) with a periodic variation of the laser light intensity [21]. While the laser-generated potential is a useful system for the study of colloidal dynamics over different potentials [21–24], the colloidal platform has several advantages in the experimental implementation. (i) It is a pure potential field and does not have any nonconservative component, as the laser beam does [50,51]. In the latter case, special arrangements need to be made in order to reduce the effect of the nonconservative forcing. (ii) Being a 2D system, the colloidal potential  $U_0(x,y)$  provides a larger sampling area, better particle statistics, and a longer equilibrium time for particles to explore different configurations without being overwhelmingly trapped to some deep minimum locations in the 1D potential. (iii) By tilting the sample at an angle  $\theta$  with respect to the vertical (gravity) direction, the tangential component of the gravitational force  $F$  used in the colloidal system can be directed to any direction in the 2D plane. The amplitude of  $F$  is well controlled and can be precisely measured without a need of calibration. The external force  $F$  used in the 1D optical trap, on the other hand, is generated by rotating the optical tweezers in a circle at a constant speed. In this case, a delicate calibration procedure is needed in order to convert the measured velocity of the particles to the force they experience [21].

## V. SUMMARY

We have carried out a systematic study of the effects of the external force  $F$  on the NESS dynamics of the diffusing particles over a tilted periodic potential, in which detailed balance is broken due to the presence of a steady particle flux  $J_{ss}$ . An analytical solution of the NESS probability density function (PDF)  $P_{ss}(x)$  is obtained from the 1D Smoluchowski

equation for the overdamped Brownian particles under the influence of a tilted periodic potential  $U(x) = U_0(x) - Fx$ . The solution reveals that the value of  $P_{ss}(x)$  at position  $x$  depends not only on the local value of  $U_0(x)$  but also on the value of  $U_0(x)$  at other positions in the period through the integration in Eq. (5). From the exact solution of the 1D Smoluchowski equation, we also obtain an analytical expression connecting the measured  $P_{ss}(x)$  with  $U_0(x)$  and  $J_{ss}$ . While no analytical solution of the 2D NESS-PDF  $P_{ss}(x,y)$  is available at the moment, we obtain the numerical results from the 2D Smoluchowski equation. In contrast to the equilibrium distribution  $P(x,y)$ , whose peak value is always located at the energy minimum, the distribution of  $P_{ss}(x,y)$  is determined by both the energy minimum and the orientation of the external force. Along the  $[1,0]$  crystalline orientation, the force  $F$  only alters the distribution of  $P_{ss}(x,y)$  along a quasi-1D path, whereas in the  $[1,1]$  crystalline orientation, the force  $F$  redistributes  $P_{ss}(x,y)$  in the entire  $x$ - $y$  plane.

To verify the analytical and numerical results, we constructed a two-layer colloidal system to study the evolution of  $P_{ss}(x,y)$  with the external force  $F$ . By tilting the entire sample at an angle  $\theta$  with respect to the vertical (gravity) direction, a tangential component of the gravitational force  $F$  is applied to the diffusing particles. In the experiment, we measured  $P_{ss}(x,y)$  when  $F$  is set in both the  $[1,0]$  and  $[1,1]$  crystalline orientations with varying amplitudes. The measured  $P_{ss}(x,y)$  in the  $[1,1]$  orientation show a good agreement with the numerical results. When the force  $F$  is along the  $[1,0]$  orientation, the particle's trajectory follows a quasi-1D zigzag path  $X$  guided by the underlying low-energy path connecting the adjacent potential wells. The quasi-1D  $P_{ss}(X)$  is then obtained from the measured  $P_{ss}(x,y)$ . The particle flux  $J_{ss}$  along the zigzag path is also measured from the particles' trajectories. With the measured  $P_{ss}(X)$  and  $J_{ss}$ , we numerically calculate the intrinsic potential  $U_0(X)$  using Eq. (8). An excellent agreement is obtained between the reconstructed potential and directly measured  $U_0(X)$  using a leveled sample. This result thus verifies our 1D theory for the NESS-PDF  $P_{ss}(x)$ .

Our work demonstrates that the tilted two-layer colloidal system is a useful platform for the study of nonequilibrium steady-state dynamics of the colloidal particles. When the external force  $F$  is not along either  $[1,0]$  or  $[1,1]$  crystal orientations, the particle flux may not follow the direction of forcing. The deflection angle between the flux and the direction of  $F$  depends on the commensurability between the particle trajectories and the underlying periodic potential. This effect has been used for particle sorting [52–54]. Recent studies also showed that the multidimensional nonequilibrium steady-state distribution determines the ratio between the transport coefficients along different primitive crystal directions [55,56]. The simulation and experimental methods used in the present study have the capability of finding the 2D steady-state distribution  $P_{ss}(x,y)$  in great detail and can certainly be applied to the further study of nonequilibrium steady-state distributions under different forcing directions. In addition to the colloidal template used in the present experiment, one may also use photolithography to create different templates of interest on a substrate in order to generate the needed 1D or 2D external potentials.

## ACKNOWLEDGMENTS

P.Y.L. thanks the Ministry of Science and Technology of Taiwan under Grant No. 101-2112-M-008-004-MY3. P.T. was supported by the Hong Kong Research Grants Council under Grant No. HKUST-16305214. P.T. and P.Y.L. also acknowledge the support in part by the Kavli Institute for Theoretical Physics China during their stay.

APPENDIX: DERIVATION OF THE 1D STEADY-STATE DISTRIBUTION  $P_{ss}(x)$ 

For notational convenience, here we define the dimensionless force  $f \equiv F\lambda/(k_B T)$  and take  $x$  to be in units of  $\lambda$ , time in units of  $\lambda^2/D_o$ , and energy in units of  $k_B T$ , so all relevant quantities are dimensionless. The flux is given by  $J(x, t) = -\partial_x P(x, t) - P(x, t)U'(x)$ , and assuming the steady-state flux  $J_{ss}$  is uniform (which is true since this is just the mean drift velocity  $v$  and was also verified in Ref. [43]), one has  $P'_{ss} + P_{ss}U' = -J_{ss}$ . Solving for  $P_{ss}$ , one has

$$P_{ss}(x) = e^{-U(x)} \left[ e^{U(0)} P_{ss}(0) - J_{ss} \int_0^x dy e^{U(y)} \right]. \quad (\text{A1})$$

For periodic solution, one has  $P_{ss}(0) = P_{ss}(1)$ , which leads to

$$J_{ss} = e^{U_0(0)} P_{ss}(0) (1 - e^{-f}) / \langle e^U \rangle, \quad \langle e^U \rangle \equiv \int_0^1 dy e^{U(y)}. \quad (\text{A2})$$

Substituting the above expression for  $J_{ss}$  back to (A1) gives

$$P_{ss}(x) = e^{U_0(0)} P_{ss}(0) e^{-U(x)} \left[ 1 - \frac{1 - e^{-f}}{\langle e^U \rangle} \int_0^x dy e^{U(y)} \right]. \quad (\text{A3})$$

Next we will show that

$$\int_0^1 dy e^{U(x+y)} + (1 - e^{-f}) \int_0^x dy e^{U(y)} = \langle e^U \rangle. \quad (\text{A4})$$

With  $z = x + y$ , the first integral on the left-hand side of (A4) becomes  $\int_x^{1+x} dz e^{U(z)}$ , and hence the left-hand side of (A4)

$$= \int_0^{1+x} dz e^{U(z)} - e^{-f} \int_0^x dy e^{U(y)}, \quad (\text{A5})$$

$$= \langle e^U \rangle + \int_1^{1+x} dz e^{U(z)} - e^{-f} \int_0^x dy e^{U(y)}, \quad (\text{A6})$$

$$= \langle e^U \rangle. \quad (\text{A7})$$

The last step follows since with  $u = z - 1$ ,  $\int_1^{1+x} dz e^{U(z)} = e^{-f} \int_0^x du e^{U(u)}$ . Since  $I_-(x) \equiv e^{-U(x)} \int_0^1 dy e^{U(x+y)}$ , thus from (A3) and (A4), one has  $P_{ss}(x) \propto I_-(x)$  and hence the steady-state distribution is

$$P_{ss}(x) = \frac{I_-(x)}{\int_0^1 I_-(x) dx}. \quad (\text{A8})$$

Finally, from (A2) and (A8), one obtains the steady-state uniform flux

$$J_{ss} = \frac{1 - e^{-f}}{\int_0^1 I_-(x) dx}. \quad (\text{A9})$$

- 
- [1] P. N. Pusey, in *Liquids, Freezing and Glass Transition*, edited by J. P. Hansen, D. Levesque, and J. Zinn-Justin (North-Holland, Amsterdam, 1991), chap. 10.
- [2] B. P. Binks and T. Horozov, *Colloidal Particles at Liquid Interfaces* (Cambridge University Press, Cambridge, UK, 2006).
- [3] P. Pieranski, *Phys. Rev. Lett.* **45**, 569 (1980).
- [4] N. D. Denkov, O. D. Velev, P. A. Kralchevsky, I. B. Ivanov, H. Yoshimura, and K. Nagayama, *Nature* **361**, 26 (1993).
- [5] T. O. E. Skinner, D. G. A. L. Aarts, and R. P. A. Dullens, *Phys. Rev. Lett.* **105**, 168301 (2010).
- [6] J. R. Savage, D. W. Blair, A. J. Levine, R. A. Guyer, and A. D. Dinsmore, *Science* **314**, 795 (2006).
- [7] Z. Zheng, F. Wang, and Y. Han, *Phys. Rev. Lett.* **107**, 065702 (2011).
- [8] Z. Zhang, N. Xu, D. T. N. Chen, P. Yunker, A. M. Alsayed, K. B. Aptowicz, P. Haddas, A. J. Liu, S. R. Nagel, and A. G. Yodh, *Nature* **459**, 230 (2009).
- [9] F. Ghezzi and J. C. Earnshaw, *J. Phys. Condens. Matter* **9**, L517 (1997).
- [10] J. Ruiz-Garcia, R. Gamez-Corrales, and B. I. Ivlev, *Phys. Rev. E* **58**, 660 (1998).
- [11] W. Chen, S. S. Tan, T. K. Ng, W. T. Ford, and P. Tong, *Phys. Rev. Lett.* **95**, 218301 (2005).
- [12] W. Chen, S. S. Tan, Z. S. Huang, T. K. Ng, W. T. Ford, and P. Tong, *Phys. Rev. E* **74**, 021406 (2006).
- [13] M. Sickert, F. Rondelez, and H. A. Stone, *Europhys. Lett.* **79**, 66005 (2007).
- [14] V. Prasad, S. A. Koehler, and E. R. Weeks, *Phys. Rev. Lett.* **97**, 176001 (2006).
- [15] Y. Peng, W. Chen, T. M. Fischer, D. A. Weitz, and P. Tong, *J. Fluid Mech.* **618**, 243 (2009).
- [16] M. H. Lee, S. P. Cardinali, D. H. Reich, K. J. Stebb, and R. L. Leheny, *Soft Matter* **7**, 7635 (2011).
- [17] W. Zhang, N. Li, K. Bohinc, P. Tong, and W. Chen, *Phys. Rev. Lett.* **111**, 168304 (2013).
- [18] J. C. Crocker and D. G. Grier, *J. Colloid Interface Sci.* **179**, 298 (1996).
- [19] X. G. Ma, P. Y. Lai, and P. Tong, *Soft Matter* **9**, 8826 (2013).
- [20] F. Reif, *Fundamentals of Statistical and Thermal Physics* (McGraw-Hill, Auckland, 1985).
- [21] V. Blicke, T. Speck, U. Seifert, and C. Bechinger, *Phys. Rev. E* **75**, 060101(R) (2007).
- [22] M. Siler and P. Zemanek, *New J. Phys.* **12**, 083001 (2010).
- [23] R. D. L. Hanes, C. Dalle-Ferrier, M. Schmiedeberg, M. C. Jenkins, and S. U. Egelhaaf, *Soft Matter* **8**, 2714 (2012).
- [24] M. P. N. Juniper, R. Besseling, D. G. A. Aarts, and R. P. A. Dullens, *Opt. Exp.* **20**, 28707 (2012).
- [25] A. Ajdari and J. Prost, *Proc. Natl. Acad. Sci. USA* **88**, 4468 (1991).

- [26] G. I. Nixon and G. W. Slater, *Phys. Rev. E* **53**, 4969 (1996).
- [27] D. C. Yeh and H. B. Huntington, *Phys. Rev. Lett.* **53**, 1469 (1984).
- [28] A. V. Latyshev, A. L. Aseev, A. B. Krasilnikov, and S. I. Stenin, *Surf. Sci.* **213**, 157 (1989).
- [29] D. Duvivier, T. D. Blake, and J. De Coninck, *Langmuir* **29**, 10132 (2013).
- [30] O. Pierre-Louis and M. I. Haftel, *Phys. Rev. Lett.* **87**, 048701 (2001).
- [31] K. Svensson, H. Olin, and E. Olsson, *Phys. Rev. Lett.* **93**, 145901 (2004).
- [32] S. Coh, W. Gannett, A. Zettl, M. L. Cohen, and S. G. Louie, *Phys. Rev. Lett.* **110**, 185901 (2013).
- [33] S. B. Smith, Y. J. Cui, and C. Bustamante, *Science* **271**, 795 (1996).
- [34] J. Liphardt, B. Onoa, S. B. Smith, I. Tinoco Jr., and C. Bustamante, *Science* **292**, 733 (2001).
- [35] M. T. Woodside, P. C. Anthony, W. M. Behnke-Parks, K. Larizadeh, D. Herschlag, and S. M. Block, *Science* **314**, 1001 (2006).
- [36] R. Merkel, P. Nassoy, A. Leung, K. Ritchie, and E. Evans, *Nature* **397**, 50 (1999).
- [37] R. Berkovich, S. Garcia-Manes, M. Urbakh, J. Klafter, and J. M. Fernandez, *Biophys. J.* **98**, 2692 (2010).
- [38] G. I. Bell, *Science* **200**, 618 (1978).
- [39] U. S. Schwarz and S. A. Safran, *Rev. Mod. Phys.* **85**, 1327 (2013).
- [40] X.-G. Ma, P.-Y. Lai, B. J. Ackerson, and P. Tong, *Soft Matter* **11**, 1182 (2015).
- [41] R. L. Stratonovich, *Radiotekh. Elektron.* **3**, 497 (1958).
- [42] P. Reimann, C. Van den Broeck, H. Linke, P. Hanggi, J. M. Rubi, and A. Perez-Madrid, *Phys. Rev. Lett.* **87**, 010602 (2001).
- [43] P. Reimann, C. Van den Broeck, H. Linke, P. Hanggi, J. M. Rubi, and A. Perez-Madrid, *Phys. Rev. E* **65**, 031104 (2002).
- [44] P. Langevin, *C. R. Acad. Sci. (Paris)* **146**, 530 (1908).
- [45] W. B. Russel, D. A. Saville, and W. R. Schowalter, *Colloidal Dispersions* (Cambridge University Press, Cambridge, UK, 1989).
- [46] C. Maes, K. Netočný, and B. M. Shergelashvili, *Phys. Rev. E* **80**, 011121 (2009).
- [47] P. Hanggi, P. Talkner, and M. Borkovec, *Rev. Mod. Phys.* **62**, 251 (1990).
- [48] Evan Evans, *Annu. Rev. Biophys. Biomol. Struct.* **30**, 105 (2001).
- [49] H. J. Lin, H. Y. Chen, Y. J. Sheng, and H. K. Tsao, *Phys. Rev. Lett.* **98**, 088304 (2007).
- [50] Y. Roichman, B. Sun, Y. Roichman, J. Amato-Grill, and D. G. Grier, *Phys. Rev. Lett.* **100**, 013602 (2008).
- [51] B. Sun, J. Lin, E. Darby, A. Y. Grosberg, and D. G. Grier, *Phys. Rev. E* **80**, 010401(R) (2009).
- [52] P. T. Korda, M. B. Taylor, and D. G. Grier, *Phys. Rev. Lett.* **89**, 128301 (2002).
- [53] L. R. Huang, E. C. Cox, R. H. Austin, and J. C. Sturm, *Science* **304**, 987 (2004).
- [54] A. M. Lacasta, J. M. Sancho, A. H. Romero, and K. Lindenberg, *Phys. Rev. Lett.* **94**, 160601 (2005).
- [55] A. Gopinathan and D. G. Grier, *Phys. Rev. Lett.* **92**, 130602 (2004).
- [56] J. Herrmann, M. Karweit, and G. Drazer, *Phys. Rev. E* **79**, 061404 (2009).